

UC San Diego

UC San Diego Previously Published Works

Title

Anomalous material-dependent transport of focused, laser-driven proton beams

Permalink

<https://escholarship.org/uc/item/9238m10x>

Journal

Scientific Reports, 8(1)

ISSN

2045-2322

Authors

Kim, J

McGuffey, C

Gautier, DC

et al.

Publication Date

2018

DOI

10.1038/s41598-018-36106-8

Copyright Information

This work is made available under the terms of a Creative Commons Attribution License, available at <https://creativecommons.org/licenses/by/4.0/>





Peer reviewed

SCIENTIFIC REPORTS



OPEN

Anomalous material-dependent transport of focused, laser-driven proton beams

J. Kim¹, C. McGuffey¹ , D. C. Gautier², A. Link³, G. E. Kemp³, E. M. Giraldez⁴, M. S. Wei⁴, R. B. Stephens⁴ , S. Kerr^{5,3}, P. L. Poole^{6,3} , R. Madden¹, B. Qiao¹, M. E. Foord³, Y. Ping³ , H. S. McLean³, J. C. Fernández² & F. N. Beg¹

Intense lasers can accelerate protons in sufficient numbers and energy that the resulting beam can heat materials to exotic warm (10s of eV temperature) states. Here we show with experimental data that a laser-driven proton beam focused onto a target heated it in a localized spot with size strongly dependent upon material and as small as 35 μm radius. Simulations indicate that cold stopping power values cannot model the intense proton beam transport in solid targets well enough to match the large differences observed. In the experiment a 74 J, 670 fs laser drove a focusing proton beam that transported through different thicknesses of solid Mylar, Al, Cu or Au, eventually heating a rear, thin, Au witness layer. The XUV emission seen from the rear of the Au indicated a clear dependence of proton beam transport upon atomic number, Z, of the transport layer: a larger and brighter emission spot was measured after proton transport through the lower Z foils even with equal mass density for supposed equivalent proton stopping range. Beam transport dynamics pertaining to the observed heated spot were investigated numerically with a particle-in-cell (PIC) code. In simulations protons moving through an Al transport layer result in higher Au temperature responsible for higher Au radiant emittance compared to a Cu transport case. The inferred finding that proton stopping varies with temperature in different materials, considerably changing the beam heating profile, can guide applications seeking to controllably heat targets with intense proton beams.

Creation of intense proton beams and their transport are active research topics due to the unique ability of such beams to volumetrically and isochorically heat matter for fundamental studies of non-equilibrium states¹ as well as materials relevant to conditions in nuclear implosions and the interior of planets^{2,3}. Other potential applications of laser-driven beams include generation of neutrons or exotic isotopes^{4,5} and the ion fast ignition inertial fusion concept^{6,7}. It has been demonstrated that protons can be accelerated to 10s of MeV via short-pulse lasers interacting with solid targets. Several different methods have been investigated for ion acceleration including the most studied mechanism target normal sheath acceleration (TNSA)^{8,9}, radiation pressure acceleration (RPA)^{10,11}, breakout after burner (BOA)^{12,13} and collisionless shock acceleration¹⁴. While proton acceleration with various mechanisms has been intensively studied, relatively few works focus on the physics arising during intense proton beam transport in various states of materials.

Early studies on proton beam transport focus on demonstration of isochoric heating of a single solid material^{15,16}. For these studies, proton beams were generated through the TNSA mechanism utilizing curved foil targets which provide the beam focusing effect as protons accelerate normal to the target toward the geometric center. When focused, these proton beams became intense enough to heat a matter sample to 10s of eV. For instance, ($>10^{11}$) protons generated from a 10 J laser were focused to a small spot ($<50 \mu\text{m}$) resulting in isochoric heating of Al foil to over 20 eV temperature¹⁵. Using a higher energy (170 J) laser, the brightest emission on Al foil corresponding to temperature of $\sim 80 \text{ eV}$ was measured¹⁶.

¹Center for Energy Research, University of California, San Diego, La Jolla CA, 92093-0417, USA. ²Los Alamos National Laboratory, Los Alamos, NM, 87545, USA. ³Lawrence Livermore National Laboratory, Livermore, CA, 94551, USA. ⁴General Atomics, San Diego, CA, 92186-5608, USA. ⁵University of Alberta, Edmonton, Alberta, T6G 2V4, Canada. ⁶Physics Department, The Ohio State University, Columbus, OH, 43210, USA. Correspondence and requests for materials should be addressed to F.N.B. (email: fbeg@ucsd.edu)

In proton beam transport, accurate accounting of how protons transfer their energy to matter as they slow down, known as proton stopping power, is one of the requirements to estimate beam projected range and heating profiles in a transport medium. For a non-relativistic proton with initial energy $>MeV$ in a metal, the stopping power and total range of the proton are dominated by electronic stopping power caused by frequent inelastic collisions with electrons. For cold materials, probabilistic yet accurate stopping power values exist for charged ions including protons, drawing from broad experimental measurements and theoretical values^{17,18}. However, model predictions for ion stopping in more complex states such as warm dense matter (WDM) or dense plasma, being neither solid nor ideal plasma, are uncertain and unverified. Major efforts to describe stopping of charged particles in this regime, a partially ionized medium, have been made via theoretical approaches and numerical calculations. One well-known approach is separately treating bound and free electrons' contributions to electronic stopping power (B + F model)^{19,20}, where fractions of these two populations are determined by plasma state conditions. A more self-consistent standard approach for charged particle stopping, the BPS model²¹, includes perturbative approaches to interactions and dynamic screening instead of simplified methods for the Coulomb energy exchange. With this model, alpha particle stopping range is predicted to be about 20–30% longer compared to most models for deuterium-tritium fusion^{22,23}. Applying the local density approximation is another well-known method²⁴. Recent calculation (SCAALP)²⁵ uses the local-density and average-atom approximations where the inhomogeneous total electron density is taken into account. Simulations using molecular dynamics²⁶ have shown that they are reasonably applicable to calculate stopping of ion transport in strongly coupled plasmas. While these approaches can calculate stopping power values, each has limitations and none is valid over a wide range of density and temperature.

Few experiments have attempted to measure proton stopping power in the WDM range because of the paradoxical situation that measurable samples are difficult to create. One measurement of stopping power was made using lower flux protons born from the D, ³He reaction to probe a laser-heated sample. The precise energy of these protons allowed for reliable comparison of the stopping calculated by various means but only for a single, high projectile velocity²⁷. The experiment was modeled with various models in a recent stopping study and found to be reproduced well using a time-dependent orbital-free density functional theory (TD-OF-DFT) method²⁸. A different experimental method was applied to make ion stopping power measurements in laser-heated warm-dense matter, but for a projectile much closer to the expected thermal velocity of the sample, where stopping power is highest and most subject to disagreement between models²⁹. The results of that experiment promote advanced stopping models including BPS and T-matrix formulation^{21,30}.

Drivers powerful enough to reach WDM conditions may cause the thermodynamic state of the sample to change rapidly, causing difficulties in predicting the behavior of the beam transport. In this case, responses of the matter and the beam to one another need to be taken into account simultaneously. Self-consistent description of intense proton beam dynamics with collective effects has been studied using PIC simulations with a B + F stopping model by this group^{31,32} and PIC with Monte Carlo stopping³³. However, these transport studies with simple stopping models are limited to a few materials and would benefit from experimental findings in relevant conditions for various materials.

In this paper, we present experimental and simulation results of proton beam transport in different solid materials with a proton beam with a fixed source. Presented first are measurements of thermal emissions due to focused beam heating. To address the experimental questions such as the cause of dependence of the emission characteristics upon transport materials and heated temperature at the rear of the target, simulations using a particle-in-cell code were carried out. Simulations of the time-dependent source are described in the second Results subsection, followed by transport simulations using the same code. Details of the experimental and computational setups are described in Methods.

Results

Experimental measurements of 68 eV emission from the target rear. A schematic diagram of the experiment and example data types are shown in Fig. 1. The TNSA proton beam generated by irradiation of the 100 TW-class Trident laser onto a Au partial-hemispherical target (“Au hemi”) with radius of curvature $r_c = 300 \mu m$ was focused as discussed below. At a distance $\sim 500 \mu m$, $\sim 1.7 \times r_c$, the focused proton beams entered then transported through solid foils having a broad range of atomic number, Z, including Mylar, Al, Cu or Au with different thicknesses and a thin Au witness layer.

The transport foil thickness for the different materials was chosen to have equivalent stopping range in cold matter using the NIST data of proton stopping¹⁸. Two series of foils were chosen. First, Mylar (CH), Al, Cu and Au had a thickness of $50 \mu m$, $30 \mu m$, $15 \mu m$ and $12.5 \mu m$, respectively, all chosen to range out $1.7 \pm 0.1 MeV$ protons. Second $13 \mu m$ Mylar and $12.5 \mu m$ Al were chosen to range out $0.9 \pm 0.1 MeV$ protons. For all materials, $0.5 \mu m$ Au layer was deposited on the rear of the transport foil to be a consistent surface for thermal emission measurements. An aluminum cylinder was fabricated to fix the distance between the Au hemi and target rear for all target types. Hot electrons generated by the laser interacting with the Au hemi can spread through the structure and reach the rear, potentially affecting the measurements. To reduce this effect, the structure was made wide ($R = 550 \mu m$) and the Au hemi was connected to it with thin support strips.

As a main measurement of beam transport, an extreme ultraviolet (XUV) imaging system imaged thermal emission from the back side of the Au layer in two dimensions. Since Planckian radiation intensity sensitively varies depending on the temperature of a material, the time integrated brightness of radiation is an indicator of the surface temperature of a target with caveats discussed later.

There are two important reference cases in the XUV dataset to consider. First, targets with no foils behind the Au hemi were shot, and bright emission was observed spread over the $300 \mu m$ Au hemi rear. The proton source was also measured in these shots. Second, a target consisting of a flat $10 \mu m$ Au target foil and Au transport foil was irradiated with the laser fully focused on the front foil to achieve highest possible intensity. The XUV

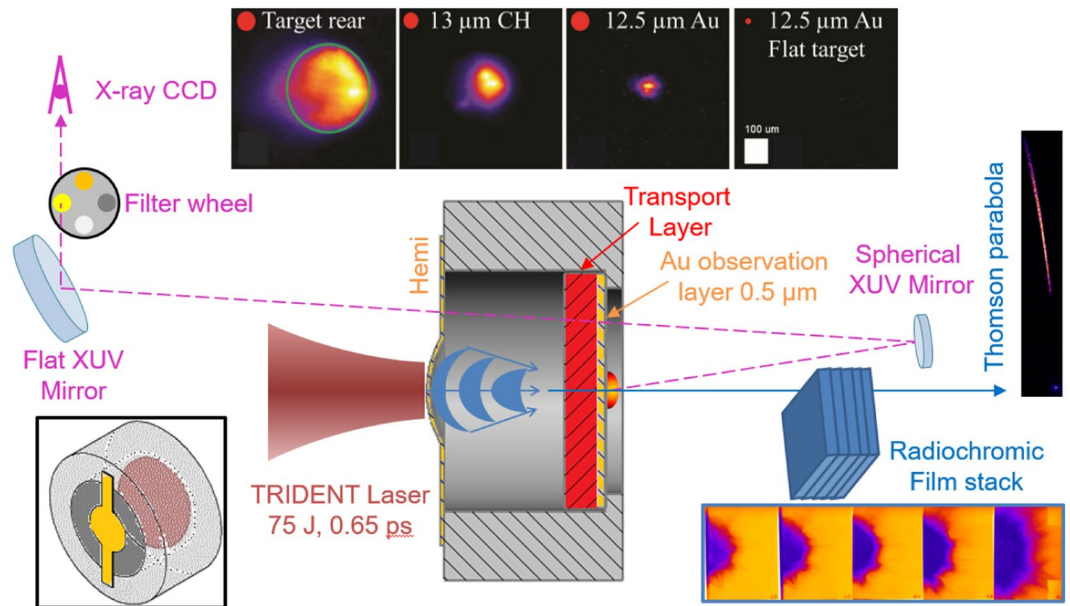


Figure 1. Diagram of experimental setup; the overall target is shown in lower left inset. The Trident short pulse laser is incident on a flat or a curved (partial hemisphere) front foil to generate the proton beam. The XUV system images thermal emission on the Au layer behind the transport foil; several examples are shown (top sequence). The red circle indicates the laser spot size on target, while the green circle is the Au hemi size. Particles are recorded nearly along the target rear normal with film (bottom series) and Thomson parabola spectrometer (right inset).

emission from the rear Au foil in this case was undetectable. This indicates that the heating from an unfocused proton beam and from any electrons that may have transited the Al structure were insufficient to heat the rear Au surface to the point of considerable 68 eV emission. Note that a typical unfocused TNSA proton beam with 50 μm source size and expansion cone angle of 20 degrees would overfill the 500 μm diameter transport foil.

For all other shots the laser irradiated target was a Au hemi. Contrary to the flat target case the XUV emitted from the surface behind the transport foil was confined locally, even smaller than the laser focus in some cases, and filters were necessary as the emission brightness was at least 3 orders of magnitude greater. This is due to the focused proton heating. Collected XUV images from different targets are shown in Fig. 1 (top series). Most interestingly, for different transport layers, the emission characteristics changed including emission size and brightness. For instance, emissions from a target with low Z material such as CH and Al were consistently larger ($>$ factor of 2) than ones with Au and Cu.

Details of emission results for all transport foils are shown in Fig. 2. Two plots present the emission size (a) and peak brightness (b) as a function of areal density, $\rho\tau$. Interestingly, all the targets with Al had a much wider emission size than targets with any other transport layer material or thickness, including those with higher atomic number and higher areal density. The largest emission size ($\sim 85 \mu\text{m}$ radius enclosing 50% XUV energy) from a target with Al is more than twice the size ($\sim 35 \mu\text{m}$) of the Au foil cases. In contrast to this strong material dependence, emission size is seen to be weakly sensitive to transport layer thickness comparing data points with the same material, but different thicknesses such as Al (open vs. closed green squares) and CH (open vs. closed blue circles). XUV peak brightness versus target $\rho\tau$ is plotted in Fig. 2(b) and is seen to have even stronger dependence than emission size. In this comparison, the dependence of emission brightness on target material (Z or $\rho\tau$) is not straightforward, but low Z materials (CH and Al) tend to show brighter signal than Cu and Au. A clear trend is that targets with the thin layer have much brighter emission ($\sim 4\times$) than their thicker counterparts having the same material.

Discrepancies exist between these experimental results and predictions of simple existing models. For example, Monte Carlo calculations³⁴ predict lateral straggling that increases with thickness but has extent of only several μm for the thicknesses investigated with thick Au being the most extreme at $\sim 12 \mu\text{m}$. As seen in the data above, the heated sizes vary by a much wider range, from 30 μm to 80 μm . Also, wider emission size for low $\rho\tau$ material is contradictory to Moliere nuclear scattering formulas³⁵ where protons traveling in high $\rho\tau$ material have wider scattering angle. Further, one might speculate that Cu and Au, having higher room temperature thermal conductivity and more free electrons than Al and CH, would experience greater lateral spreading of the heat deposited via proton stopping, heating a wider portion of the Au emission surface. However, the data oppose all these trends with Cu and Au cases having the smallest emission regions. For these results, it can be concluded that transport for dense proton beams cannot be explained by only cold stopping and scattering models. Particle-in-cell (PIC) computational modeling of the proton beam transport with fields and an advanced model for proton electronic stopping power^{31,32} was conducted to aid in the interpretation of experimental observation

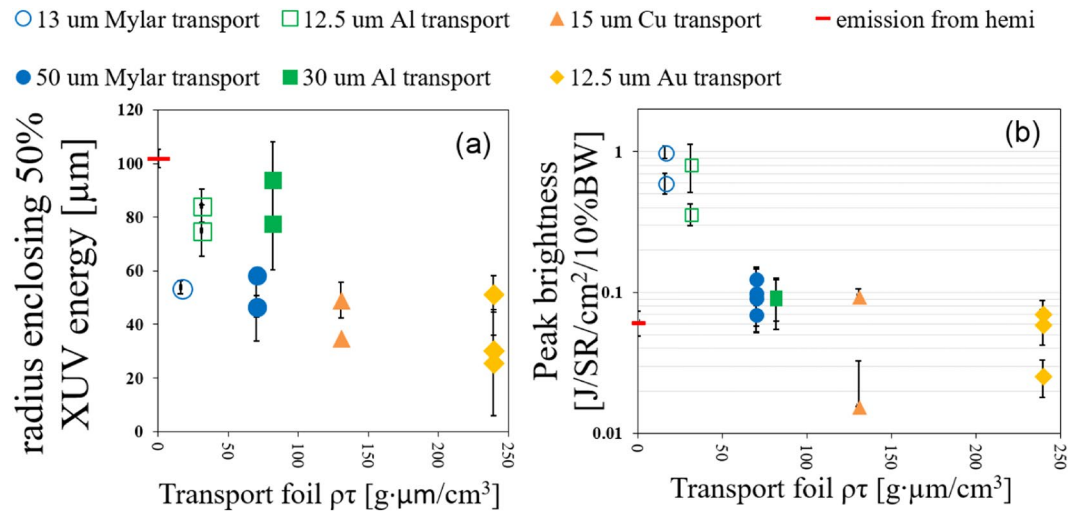


Figure 2. XUV emissions observed from the Au layer behind a transport foil of different materials and thicknesses. Each data point represents a single shot. Areal density of target versus XUV emission size (a) and XUV peak brightness (b). The red dash point plots the case of a target with neither Au nor transport foil so that the rear of the Au hemi was visible. The error bars in (a) are the difference between the vertical and horizontal FWHM. The error bars in (b) include the laser energy variation and the range of two different peak analysis approaches.

as described in the following section. It will be shown that the nonlinear dependence of emissivity versus temperature must also be taken into account in understanding these experimental results.

Simulating a parameterized proton beam source using particle-in-cell LSP. Simulation of the experiment was conducted using particle-in-cell code LSP³⁶. Simulating the configuration at full scale would require ~ 40 ps simulation run time at great computational expense so that the entire beam including low energy ~ 1 MeV protons can traverse the transport and witness foils positioned $450 \mu\text{m}$ behind the hemi. Moreover, this simulation would need to be repeated for different transport materials. Thus, to efficiently use computational resources, the problem was divided into two steps. First, proton beam generation and drift was modeled and compared to the measured spectrum. The resulting proton beam source was then used in a second series of transport simulations. Details of the simulations are given in the Methods section.

The source simulation was performed by injecting a population of electrons with parameters based on the measured laser qualities at the laser interaction location on the hemi. The target geometry was reconstructed in 2D Cartesian coordinates and a kinetic hydrogen species was initialized on the hemi rear. Electrons quickly spread out from the front side of the hemi target and expanded into the vacuum away from surfaces, driving a typical TNSA sheath field. At the rear side of the hemi, this field was strong enough (> 1 TV/m) to accelerate protons to MeV energy. Those protons initially accelerated normal to the target (moving toward the target geometric center) then expanded transversely by radial fields generated in the beam. Figure 3(a) presents a snapshot of proton density at 20 ps.

Critically, it was observed from the proton generation simulation that the proton source could not be well parameterized with single fixed values. Two main characteristics of the proton beam are (i) proton energy distribution varied with time and (ii) the beam spatial profile at the extraction plane was different for differing proton energies. Figure 3(b) shows the time integrated proton energy spectrum for two time intervals (time integrated up to 10 ps and from 10 to 20 ps) measured at the extraction plane ($z = 400 \mu\text{m}$ where z is the longitudinal axis). Fast moving protons (the early time group, arriving during the 0 to 10 ps interval) present a higher slope temperature, while those arriving later (10–20 ps) had a lower slope temperature. The second characteristic of the proton beam is that higher energy protons are focused to a small waist when they reach the extraction plane, whereas lower energy protons are uniformly spread over a larger radial area. For these reasons, it was decided that the beam entering the transport layers could not be represented by a beam with a steady-state, single characteristic spectrum, nor single size. Instead, the early and late protons were fit to two beams with duration, total energy, size and characteristic slope temperature given in Fig. 4 and its caption.

Hybrid PIC simulations of particle transport through self-consistently heated transport layers. To study transport in the foil layers, one key factor is particle stopping power, which determines how much energy particles lose and ultimately where they stop in the medium. The same PIC code was used in a different mode to study transport in the secondary target. While the PIC algorithm precludes explicit binary collisions, quantum and atomic-scale effects cannot directly be included. However, this code can allow new understandings into intense beam transport due to an included dynamic proton stopping power module³¹ that updates according to the thermodynamic state of the material locally. Cases were also run with cold stopping¹⁸ for comparison. Two materials were chosen, Al and Cu, since in the experiment these transport materials exhibited dramatically different features of XUV emissions. Two proton beams were injected sequentially into the transport material with beam input parameters according to the representative fits discussed in the previous section. The total energy in both beams is 1.2 J, which is about 1.5% of the laser energy used in the experiment. Details can again be found in Methods.

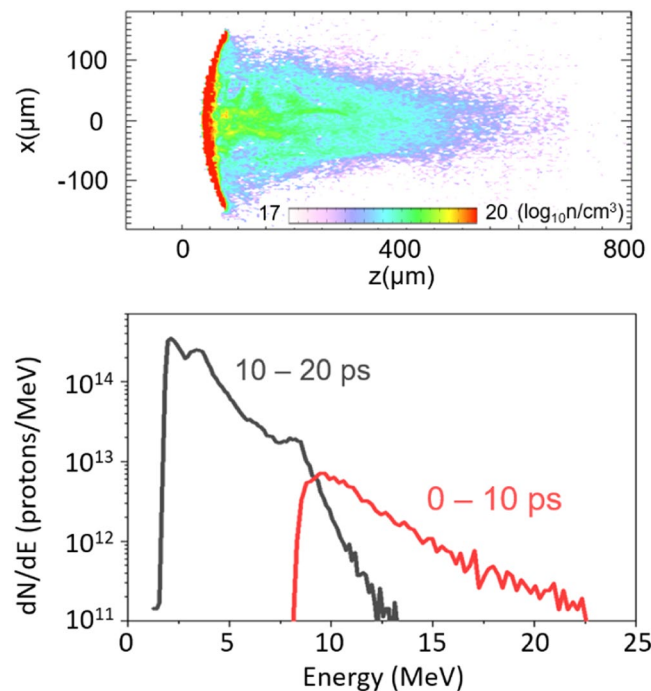


Figure 3. (a) Snapshot of protons generated from a partial-hemi target in the PIC source simulation. The energy spectrum of protons collected at $z = 400 \mu\text{m}$ in the first or second 10 ps period (b).

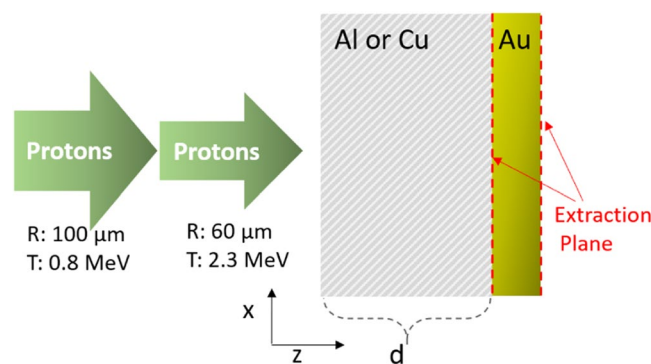


Figure 4. Domain schematic of the transport simulations. Two proton beams with different parameters are sequentially injected inside a transport layer whereby standoff distance from the Au layer, d , varies with material; Al case: $30 \mu\text{m}$ and Cu case: $15 \mu\text{m}$. Proton beams injected earlier and (later) are characterized with slope temperature of 2.3 MeV (0.8 MeV), pulse energy of 0.45 J (0.75 J), pulse duration of 7 ps (13 ps) and gaussian spatial profile with $60 \mu\text{m}$ radius (flat profile with $100 \mu\text{m}$ radius).

Figure 5 shows results of the transport simulations. Proton numbers and proton energy fluence counted at the first extraction planes, time-integrated until all protons leave the transport layer (Al or Cu) are shown in Fig. 5(a,b). From Fig. 5(a), it can be seen that more protons pass through the Al than the Cu layer. Interestingly, the difference is greater far from the central beam axis, in the lateral wings where mostly lower energy protons were injected. Similarly, a higher proton energy fluence is shown in the case of the Al transport layer. In contrast, when the fixed stopping power (cold stopping from NIST) is applied for both Al and Cu layers in simulations, energy fluences for both cases are nearly overlapped (dashed lines). Because the thicknesses ($30 \mu\text{m}$ and $15 \mu\text{m}$) of the two layers were determined by cold stopping range (for a proton of 1.7 MeV), similar energy fluences are expected. Varied energy fluence in the dynamic stopping simulation indicates that protons traveling in Al lose proportionally less energy than the Cu case as proton stopping power changes with the thermodynamic states of the transport layer. This result informs us that choice of a dynamic, or at least non-room-temperature stopping power model is necessary to reproduce the differences in proton transport observed in the experiment.

Total proton energy fluences deposited in the Au layer are found by the energy lost by particles between the Au entrance and exit extraction planes. Particles that were counted in the entrance extraction plane but not the

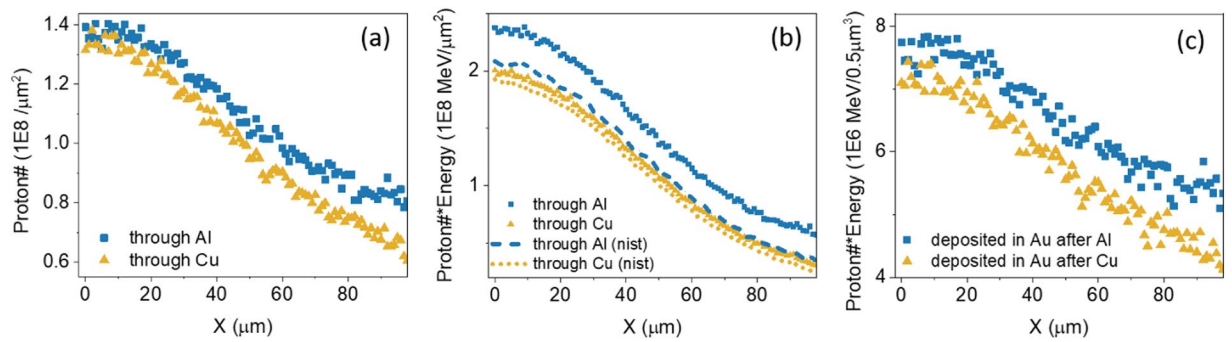


Figure 5. Time-integrated proton number (a) and proton energy (b) fluence profiles in the x-axis measured at the exit of the transport layer ($30\ \mu\text{m}$ Al or $15\ \mu\text{m}$ Cu). The bin width for both dimensions is $1\ \mu\text{m}$. (b) Includes proton energy fluence results obtained using the dynamic stopping power and cold stopping power (NIST) for comparison. (c) Shows the time integrated proton energy fluence that is deposited in the Au layer (up to $0.5\ \mu\text{m}$).

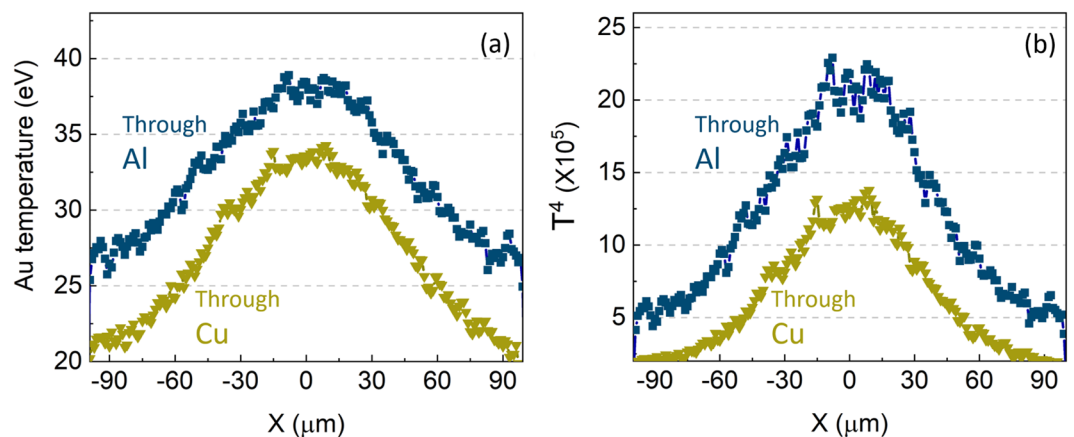


Figure 6. Spatial temperature profile (a) and the fourth power of temperature (b) of Au target at $0.5\ \mu\text{m}$ depth for both Al and Cu cases.

exit plane were assumed to deposit all their energy in the entrance bin. The deposited fluence curves are shown in Fig. 5.

Here, the heated temperature of Au can be estimated using the deposited energy fluence. For instance, energy fluence through the Al layer is $\sim 7.5 \times 10^6\ \text{MeV}/\mu\text{m}^2$ at the first bin ($0\text{--}1\ \mu\text{m}$) in x-axis corresponding to a volume of $0.5 \times 1 \times 1\ \mu\text{m}^3$. Using the volumetric heat capacity of Au, $2.43 \times 10^{-12}\ \text{J}/\text{K}\mu\text{m}^3$, the calculated Au temperature is $40\ \text{eV}$. This estimation is similar to the simulation result as shown in Fig. 6(a) where peak temperatures at a central region for both Al and Cu cases are $\sim 38\ \text{eV}$ and $33\ \text{eV}$ respectively.

Using XUV emission brightness as a temperature diagnostic has caveats. A radiating blackbody with temperature $14\ \text{eV}$ has a peak in spectral radiance at $68\ \text{eV}$. This means that the response of the imaging system is not linear and can exaggerate the cooler regions further out from the spot. Additionally, emittance is strongly dependent on temperature. The Stefan-Boltzmann law describes the total power of black-body radiation depending on the object's temperature with the relation $j = \sigma T^4$, where j , σ and T are respectively the radiated emittance, Stefan-Boltzmann constant and temperature. While this does not hold true for a single photon band, its scaling shows how a temperature difference of just $5\ \text{eV}$ can lead to a large difference of radiated emittance. As shown in Fig. 6(b), the fourth power of each temperature of 38 and 33 becomes $\sim 2.1\text{e}6$ and $\sim 1.2\text{e}6$ respectively. The ratio of these values is lower than experimental measurement where $>2\times$ higher XUV brightness was measured from the Al case compared to the Cu case. However, this modeling treatment reproduces the direction of the trend of XUV brightness from the two different materials.

An important feature is the relatively gradual lateral temperature gradient in the Al case compared to the Cu case. This trend is clearly seen particularly for the outer part in the transverse direction (x-axis), leading to $>2\times$ higher emission brightness for the Al case. The XUV imaging has a limitation for measuring emission brightness because the target emitting XUV expands rapidly, resulting in the reduction of absolute brightness. For example, previous work using LASNEX (radiative-hydrodynamics code) simulation³⁷ predicted that the XUV brightness corresponding to a Cu target temperature below $\sim 20\ \text{eV}$ is hardly detectable. Considering this limit, it can be inferred that the Al case has a broader area over which XUV emission can be detected. For Al and Cu layers, ranges (X-axis) for temperature above $30\ \text{eV}$ are $130\ \mu\text{m}$ and $70\ \mu\text{m}$, respectively; for temperature above $25\ \text{eV}$ they are $200\ \mu\text{m}$ and $120\ \mu\text{m}$ respectively. This difference in size of the signal in simulations has the same trend

observed in the experiment where emission size ($R \sim 80 \mu\text{m}$) for Al target is about twice that from a Cu target. Note that the beam central area is heated by two characterized beams, but only the second beam (low energy protons) is involved in heating of the wings. Thus, an inference can be drawn that low energy protons are responsible for the clear distinction in heating profile at the wings for the two different material cases.

Additionally, the induced magnetic field during proton beam transport was measured in the simulation to see if the magnetic field had any influence on beam profiles in different materials. However, the proton beam was not intense enough to produce high magnetic fields, (the maximum magnetic field is below 10 Tesla for a given proton beam) and it cannot affect the beam transport in the low thicknesses used.

Discussion

In this work, the experiments showed that the size and brightness of XUV emissions caused by proton beams vary by a factor of >2 with the target material, demonstrating an unexpectedly strong dependence of proton beam transport on materials.

Simulation modeling of the experiments showed that protons moving through an Al transport layer heat the rear of Au to higher temperature resulting in higher radiated emittance compared to a Cu transport case. This result is consistent with the experimental measurement showing the different brightness of XUV between two material cases. Higher temperature over an entire area of Au for the Al case helps explain the brighter and wider XUV emission size seen from the experiment. These results provide an understanding that the variation of stopping power with temperature in different materials can considerably change the beam heating profile in targets. This effect turned out to be dominant rather than other effects such as beam scattering and induced weak magnetic field for the pertinent proton beam density.

In the range of target temperature ($<40 \text{ eV}$) encountered in this work, change of stopping power is relatively considerable only for protons having energies below 1 MeV. Thus it can be inferred that low energy protons played an important role in varying heating profiles in different materials with given thicknesses. Currently, stopping power models for low energy protons in CH or Au materials are limited and unvalidated, inhibiting the range of our investigation. More accurate stopping models in this regime would help us carry out further investigations of the physics of intense beam transport in solids.

Methods

Laser, targets, and diagnostics. The experiments were conducted using the Trident laser facility at Los Alamos National Laboratory. Chirped pulse amplified laser pulses delivered an energy of $74 \pm 7 \text{ J}$ on a target in a duration of $670 \pm 50 \text{ fs}$ with an incidence angle of 22.5° . The spectral phase and pulse shape of the laser have been carefully characterized by the facility³⁸ through frequency resolved optical gating (FROG). Measurements were taken with a spectrometer and a FROG on most shots in this experiment of the pulse leaving the compressor as well as the pulse reflected from the target. The laser spot was characterized by relaying an image onto a CCD at low laser power. The spot at the target apex plane contained 50% of the laser energy within $65 \mu\text{m}$, achieved by deliberately defocusing to uniformly cover a large area of a target with the desired outcome that doing so can aid beam focusing by the TNSA mechanism with a curved target^{39,40}. The intensity was $3 \pm 0.5 \times 10^{18} \text{ W/cm}^2$. No attempt was made to measure or mitigate spatio-temporal coupling effects⁴¹ which, if present, would equally affect all shots. Similarly, non-uniformities in the defocused laser spot, which are known to manifest in the proton beam⁴², are presumed to affect the proton source equally for all shots. The $10 \mu\text{m}$ Au hemi was chosen as the proton source target because experience has shown it to be reliable and relatively free from instability-induced structures in the proton beam profile.

To measure the energy spectrum of generated protons, a stack of radiochromic films (RCF) and Thomson Parabola (TP) were used on each shot; for the electron spectrum, a magnetic spectrometer was fielded just below the TP line of sight. In the XUV imaging system³⁷, the first optic was a spherical mirror with 50 cm radius of curvature, r_{curv} , consisting of 21 pairs of Mo_2C and Si layers. It was placed 20 degrees off the target rear normal at a distance of 27.6 cm , where it reflected 68 eV light to a second, flat mirror in a turning chamber and imaged it onto a CCD filtered with Al.

Simulations. Modeling was conducted using the implicit, hybrid, particle-in-cell code LSP³⁶. The simulation method used here to model the TNSA mechanism is to inject relativistic electrons that are representing those accelerated by laser interaction with a target^{40,43}. For this injection, electrons of $T_e = 0.5 \text{ MeV}$ distribution with 650 fs duration were chosen, based on the fast electron spectrum measured with an electron spectrometer during the experiment as well as a reasonable agreement to the Beg and Ponderomotive scalings^{44,45} for the Trident laser parameters. Energy coupling from laser to electron was assumed to be 20%⁴⁶. In a 2D cartesian simulation, both Au ions and electrons in a partial hemi with the same size as the real Au target are treated as a fluid, and a kinetic hydrogen layer is positioned at the rear of the hemi target.

In the proton transport simulations, both ions and electrons for materials are set up as fluid where their ionization and heating capacity are updated from the equation of state tables produced by PROPACEOS⁴⁷. Although PIC simulations have limits to provide accurate interpretation of quantum phenomenon for warm dense matter, many effects for proton beam transport are self-consistently modeled with dynamic stopping calculation which is based on matter's local thermodynamic states (density, temperature, and charge distributions.) Also fields evolution is determined by both beam current and matter's local resistivity change. Electrons co-moving with protons in the TNSA beam have an energy of only several keV, stopping at the target front surface. As their impact on the transport is negligible, only protons were sent to the target in these simulations. Once protons travel through a transport layer (Al or Cu) up to distance $d = 30 \mu\text{m}$ and $15 \mu\text{m}$ respectively, the proton data including particle energy (3 dimensions in velocity space) and positions in 2D are recorded in the extraction plane and re-injected from that plane into an Au target. The last extraction plane is positioned at $0.5 \mu\text{m}$ inside the Au as following the

experiment where 0.5 μm Au layer was coated at back surface of transport foil. In these simulations, dynamic proton stopping power³¹ that is updated based on its thermodynamic state at each time step was applied for Al and Cu. For Au medium, only cold stopping was applied due to a limit of using an equation of state that is required for dynamic stopping calculation.

Data Availability

The datasets generated during and/or analyzed during the current study are available on reasonable request to F. N. Beg (fbeg@ucsd.edu) and C. McGuffey (cmcguffey@ucsd.edu).

References

- White, T. G. *et al.* Observation of inhibited electron-ion coupling in strongly heated graphite. *Sci. reports* **2**, 889, <https://doi.org/10.1038/srep00889> (2012).
- Pelka, A. *et al.* Ultrafast melting of carbon induced by intense proton beams. *Phys. Rev. Lett.* **105**, 265701 (2010).
- White, T. G. *et al.* Electron-ion equilibration in ultrafast heated graphite. *Phys. Rev. Lett.* **112**, 145005 (2014).
- Higginson, D. P. *et al.* Production of neutrons up to 18 mev in high-intensity, short-pulse laser matter interactions. *Phys. Plasmas* **18**, 100703 (2011).
- Petrov, G. M. *et al.* Generation of high-energy (>15 mev) neutrons using short pulse high intensity lasers. *Phys. Plasmas* **19**, 093106 (2012).
- Fernandez, J. C. *et al.* Fast ignition with laser-driven proton and ion beams. *Nucl. Fusion* **54**, 054006 (2014).
- Roth, M. *et al.* Fast ignition by intense laser-accelerated proton beams. *Phys. Rev. Lett.* **86**, 436–439 (2001).
- Wilks, S. C. *et al.* Energetic proton generation in ultra-intense laser–solid interactions. *Phys. Plasmas* **8**, 542 (2001).
- Snively, R. A. *et al.* Intense high-energy proton beams from petawatt-laser irradiation of solids. *Phys. Rev. Lett.* **85**, 2945 (2000).
- Esirkepov, T., Borghesi, M., Bulanov, S. V., Mourou, G. & Tajima, T. Highly efficient relativistic-ion generation in the laser-piston regime. *Phys. Rev. Lett.* **92**, 175003 (2004).
- Schlegel, T. *et al.* Relativistic laser piston model: Ponderomotive ion acceleration in dense plasmas using ultraintense laser pulses. *Phys. Plasmas* **16**, 083103 (2009).
- Yin, L. *et al.* Mono-energetic ion beam acceleration in solitary waves during relativistic transparency using high-contrast circularly polarized short-pulse laser and nanoscale targets. *Phys. Plasmas* **18**, 053103 (2011).
- Daido, H., Nishiuchi, M. & Pirozhkov, A. S. Review of laser-driven ion sources and their applications. *Rep. Prog. Phys.* **75**, 056401 (2012).
- Fiuza, F. *et al.* Laser-driven shock acceleration of monoenergetic ion beams. *Phys. Rev. Lett.* **109**, 215001 (2012).
- Patel, P. K. *et al.* Isochoric heating of solid-density matter with an ultrafast proton beam. *Phys. Rev. Lett.* **91**, 125004 (2003).
- Snively, R. A. *et al.* Laser generated proton beam focusing and high temperature isochoric heating of solid matter. *Phys. Plasmas* **14**, 092703 (2007).
- Ziegler, J. F. Stopping of energetic light ions in elemental matter. *J. Appl. Phys.* **85**, 1249 (1999).
- Berger, M. J., Coursey, J. S., Zucker, M. A. & Chang, J. PSTAR: stopping-power and range tables for protons. National Institute of Standards and Technology, Gaithersburg, MD, USA. <http://physics.nist.gov/physrefdata/star/text/pstar.html> (2005).
- Zimmerman, G. B. Recent developments in Monte Carlo techniques LLNL Tech. Rep. UCRL-JC-105616 (1990).
- Mehlhorn, T. A. A finite material temperature model for ion energy deposition in ion driven inertial confinement fusion targets. *J. Appl. Phys.* **52**, 6522 (1981).
- Brown, L. S., Preston, D. L. & Singleton, R. L. Jr. Charged particle motion in a highly ionized plasma. *Phys. Reports*. **410**, 237–333 (2005).
- Singleton, R. L. Charged particle stopping power effects on ignition: Some results from an exact calculation. *Phys. Plasmas* **15**, 056302, <https://doi.org/10.1063/1.2840134> (2008).
- Li, C.-K. & Petrasso, R. D. Charged-particle stopping powers in inertial confinement fusion plasmas. *Phys. Rev. Lett.* **70**, 3059–3062, <https://doi.org/10.1103/PhysRevLett.70.3059> (1993).
- Wang, P., Mehlhorn, T. M. & MacFarlane, J. J. A unified self-consistent model for calculating ion stopping power in icf plasma. *Phys. Plasmas* **5** (1998).
- Faussurier, G., Blancard, C., Cosse, P. & Renaudin, P. Equation of state, transport coefficients, and stopping power of dense plasmas from the average-atom model self-consistent approach for astrophysical and laboratory plasmas. *Phys. Plasmas* **17**, 052707 (2010).
- Grabowski, P. E., Surh, M. P., Richards, D. F., Graziani, F. R. & Murillo, M. S. Molecular dynamics simulations of classical stopping power. *Phys. Rev. Lett.* **111**, 215002 (2013).
- Zylstra, A. B. *et al.* Measurement of charged-particle stopping in warm dense plasma. *Phys. Rev. Lett.* **114**, 215002 (2015).
- Ding, Y. H. *et al.* Ab initio studies on the stopping power of warm dense matter with time-dependent orbital-free density functional theory. *Phys. Rev. Lett.* **121**, 145001 (2018).
- Cayzac, W. *et al.* Experimental discrimination of ion stopping models near the Bragg peak in highly ionized matter. *Nat. Commun.* **8**, 15693, <https://doi.org/10.1038/ncomms15693> (2017).
- Gericke, D. O. & Schlages, M. Beam-plasma coupling effects on the stopping power of dense plasmas. *Phys. Rev. E* **60**, 904–910, <https://doi.org/10.1103/PhysRevE.60.904> (1999).
- Kim, J. *et al.* Self-consistent simulation of transport and energy deposition of intense laser-accelerated proton beams in solid-density matter. *Phys. Rev. Lett.* **115**, 054801 (2015).
- Kim, J. *et al.* Varying stopping and self-focusing of intense proton beams as they heat solid density matter. *Phys. Plasmas* **23**, 043104 (2016).
- Wu, D., He, X. T., Yu, W. & Fritzsche, S. Monte carlo approach to calculate proton stopping in warm dense matter within particle-in-cell simulations. *Phys. Rev. E* **95**, 023207 (2017).
- Ziegler, J. F. TRIM: the transport of ions in matter. <http://www.srim.org> (2013).
- Bethe, H. A. Molière's theory of multiple scattering. *Phys. Rev.* **89**, 1256–1266 (1953).
- Welch, D. R., Rose, D. V., Cuneo, M. E., Campbell, R. B. & Mehlhorn, T. A. Isp. *Phys. Plasmas* **13**, 063105 (2006).
- Ma, T. *et al.* Determination of electron-heated temperatures of petawatt laser-irradiated foil targets with 256 and 68 ev extreme ultraviolet imaging. *Rev. Sci. Instruments* **79**, 093507 (2008).
- Palaniyappan, S. *et al.* Pulse shape measurements using single shot-frequency resolved optical gating for high energy (80j) short pulse (600 fs) laser. *Rev. Sci. Instruments* **81**, 10E103, <https://doi.org/10.1063/1.3464258> (2010).
- Bartal, T. *et al.* Focusing of short-pulse high-intensity laser-accelerated proton beams. *Nat. Phys.* **7**, 2153 (2011).
- Foord, M. E. *et al.* Proton trajectories and electric fields in a laser-accelerated focused proton beam. *Phys. Plasmas* **19**, 056702 (2012).
- Kahaly, S. *et al.* Investigation of amplitude spatio-temporal couplings at the focus of a 100 tw-25 fs laser. *Appl. Phys. Lett.* **104**, 054103, <https://doi.org/10.1063/1.4863828> (2014).
- Aurand, B. *et al.* Manipulation of the spatial distribution of laser-accelerated proton beams by varying the laser intensity distribution. *Phys. Plasmas* **23**, 023113, <https://doi.org/10.1063/1.4942032> (2016).

43. Qiao, B. *et al.* Dynamics of high-energy proton beam acceleration and focusing from hemisphere-cone targets by high-intensity lasers. *Phys. Rev. E* **87**, 013108, <https://doi.org/10.1103/PhysRevE.87.013108> (2013).
44. Beg, F. N. *et al.* A study of picosecond laser-solid interactions up to 10^{19} w cm⁻². *Phys. Plasmas* **4**, 447–457 (1997).
45. Wilks, S. C., Kruer, W. L., Tabak, M. & Langdon, A. B. Absorption of ultra-intense laser pulses. *Phys. Rev. Lett.* **69**, 1383–1386 (1992).
46. Chen, C. D. *et al.* Bremsstrahlung and k-alpha fluorescence measurements for inferring conversion efficiencies into fast ignition relevant hot electrons. *Phys. Plasmas* **16**, 082705 (2009).
47. MacFarlane, J. J., Golovkin, I. E. & Woodruff, P. R. PrOpacEOS: Equation Of State and multigroup opacity data utilized by radiation-hydrodynamics simulation codes. PRISM Computational Sciences, Wisconsin, USA. www.prism-cs.com/software/propaceos/overview.html (2016).

Acknowledgements

The authors thank the TRIDENT laser staff, R.P. Johnson, T. Shimada, R. Gonzales, and S. Reid and facility personnel S. Palaniyappan, D. Jung, and D.S. Montgomery for their dedication to the reliable operation of the facility. T. Ma and T. Bartal provided useful discussions. This work was performed under the auspices of the U.S. Department of Energy under Contract DE-AC52-07NA27344, DE-SC0001265, and DE-SC0014600. C.M. acknowledges support by the US AFOSR YIP award FA9550-14-1-0346.

Author Contributions

F.N.B., M.S.W. and C.M. designed the experiment. E.M.G., R.B.S., M.S.W., and C.M. developed the target concept and led fabrication. C.M. and D.C.G. led the experiment with support from J.K., A.L., G.E.K., M.S.W., S.K., P.P., R.M., Y.P., and H.S.M. J.C.F. and F.N.B. coordinated the project. The simulations were carried out by J.K. with guidance from M.E.F. and B.Q. The manuscript was written by J.K., C.M. and F.N.B.

Additional Information

Competing Interests: The authors declare no competing interests.

Publisher's note: Springer Nature remains neutral with regard to jurisdictional claims in published maps and institutional affiliations.



Open Access This article is licensed under a Creative Commons Attribution 4.0 International License, which permits use, sharing, adaptation, distribution and reproduction in any medium or format, as long as you give appropriate credit to the original author(s) and the source, provide a link to the Creative Commons license, and indicate if changes were made. The images or other third party material in this article are included in the article's Creative Commons license, unless indicated otherwise in a credit line to the material. If material is not included in the article's Creative Commons license and your intended use is not permitted by statutory regulation or exceeds the permitted use, you will need to obtain permission directly from the copyright holder. To view a copy of this license, visit <http://creativecommons.org/licenses/by/4.0/>.

© The Author(s) 2018